

<b>REPORT DOCUMENTATION PAGE</b>		<b>Form Approved</b> <b>OMB No. 0704-0188</b>	
<small>Public reporting burden for this collection of information is estimated to average 1 hour per response, including the time for reviewing instructions, searching data sources, gathering and maintaining the data needed, and completing and reviewing the collection of information. Send comments regarding this burden estimate or any other aspect of this collection of information, including suggestions for reducing this burden to Washington Headquarters Service, Directorate for Information Operations and Reports, 1215 Jefferson Davis Highway, Suite 1204, Arlington, VA 22202-4302, and to the Office of Management and Budget, Paperwork Reduction Project (0704-0188) Washington, DC 20503.</small>			
<b>PLEASE DO NOT RETURN YOUR FORM TO THE ABOVE ADDRESS.</b>			
<b>1. REPORT DATE (DD-MM-YYYY)</b> 2/15/01		<b>2. REPORT Type</b> Final Report	
<b>3. DATES COVERED (From - To)</b> 4/1/97 - 9/30/98		<b>4. TITLE AND SUBTITLE</b>  Computational and Experimental Investigation of Air Vehicle Aeromechanics During Shipboard Dynamic Interface Operations	
<b>5a. CONTRACT NUMBER</b>		<b>5b. GRANT NUMBER</b> N00014-97-1-0530	
<b>5c. PROGRAM ELEMENT NUMBER</b>		<b>5d. PROJECT NUMBER</b>	
<b>5e. TASK NUMBER</b>		<b>5f. WORK UNIT NUMBER</b>	
<b>6. AUTHOR(S)</b>  Dr. Edward Smith Dr. Lyle Long		<b>7. PERFORMING ORGANIZATION NAME(S) AND ADDRESS(ES)</b>  Penn State University Aerospace Engineering 233 Hammond Building University Park, PA 16802	
<b>8. PERFORMING ORGANIZATION REPORT NUMBER</b>		<b>9. SPONSORING/MONITORING AGENCY NAME(S) AND ADDRESS(ES)</b>  US Department of the Navy Office of Naval Research Ballston Centre Tower One 800 North Quincy Street Arlington, VA 22217-5660	
<b>10. SPONSOR/MONITOR'S ACRONYM(S)</b>  ONR		<b>11. SPONSORING/MONITORING AGENCY REPORT NUMBER</b>	
<b>12. DISTRIBUTION AVAILABILITY STATEMENT</b>  Unlimited Distribution			
<b>13. SUPPLEMENTARY NOTES</b>			
<b>14. ABSTRACT</b>  An analysis has been developed to predict transient aeroelastic response of gimbaled tiltrotors during shipboard engage/disengage operations. The blades are modeled as slender elastic beams attached to a gimbaled rotor hub undergoing flap and lag bending, elastic twist, and axial deflection. The gimbal restraint is simulated using a conditional rotational spring. The rotor equations of motion are formulated using Hamilton's principle and spatially discretized using the finite element method. The discretized equations of motion are integrated in time for a specified rotor speed profile. Blade element theory is used to calculate quasi-steady loads in linear and nonlinear regimes. Studies for a 1/5 <sup>th</sup> -size aeroelastically scaled tiltrotor are conducted to validate the analysis and investigate transient response and loads. Good correlation existed between the experimental data and the prediction of blade flap and lag moments in a hover condition. Blade bending moment and hub moment predictions indicated that gimbal restraint impacts could induce high transient loads on the rotor blades and hub. A new method for simulating ship airwake flow fields is presented. Ship airwake flow fields are inherently unsteady and very difficult to predict with numerical tools. The method presented in this paper is called the Nonlinear Disturbance Equations (NLDE) and is fourth order accurate in both space and time. In this method the steady state flow field is solved first, and then the unsteady fluctuations are solved. Steady and unsteady results are presented for a generic frigate shape. The parallel method is a necessity for ship airwake problems and MPI is used in the NLDE solver. Comparison of the parallel performance on various computers is also presented.			
<b>15. SUBJECT TERMS</b>			
<b>16. SECURITY CLASSIFICATION OF:</b>		<b>17. LIMITATION OF ABSTRACT</b>	<b>18. NUMBER OF PAGES</b>
<b>a. REPORT</b> U	<b>b. ABSTRACT</b> U	<b>c. THIS PAGE</b> U	UU 24
<b>19a. NAME OF RESPONSIBLE PERSON</b> Dr. Edward Smith			<b>19b. TELEPHONE NUMBER (include area code)</b> (814) 863-0966



February 20, 2001

Office of Naval Research  
Program Officer Patrick Purtell ONR 333  
Ballston Centre Tower One  
800 North Quincy Street  
Arlington, VA 22217-5660

Dear Dr. Purtell,

The enclosed information is in regard to the support of Grant N00014-97-1-0530. The following is enclosed:

1. SF-298 form
2. Report – Computational And Experimental Investigation of Air Vehicle Aeromechanics During Shipboard Dynamic Interface Operations

Please add this information to what you already have for the final report. Sorry for the delay in providing you this information.

Thanks very much for your support.

Sincerely,

Edward Smith  
Associate Professor of  
Aerospace Engineering

Enclosure

Cc Debra Huber

# **Computational and Experimental Investigation of Air Vehicle Aeromechanics During Shipboard Dynamic Interface Operations**

**Dates: 4/1/97 -9/30/98  
Grant #: N00014-97-1-0530**

## **Abstract**

**An analysis has been developed to predict transient aeroelastic response of gimballed tiltrotors during shipboard engage/disengage operations. The blades are modeled as slender elastic beams attached to a gimballed rotor hub undergoing flap and lag bending, elastic twist, and axial deflection. The gimbal restraint is simulated using a conditional rotational spring. The rotor equations of motion are formulated using Hamilton's principle and spatially discretized using the finite element method. The discretized equations of motion are integrated in time for a specified rotor speed profile. Blade element theory is used to calculate quasi-steady loads in linear and nonlinear regimes. Studies for a 1/5<sup>th</sup>-size aeroelastically scaled tiltrotor are conducted to validate the analysis and investigate transient response and loads. Good correlation existed between the experimental data and the prediction of blade flap and lag moments in a hover condition. Blade bending moment and hub moment predictions indicated that gimbal restraint impacts could induce high transient loads on the rotor blades and hub. A new method for simulating ship airwake flow fields is presented. Ship airwake flow fields are inherently unsteady and very difficult to predict with numerical tools. The method presented in this paper is called the Nonlinear Disturbance Equations (NLDE) and is fourth order accurate in both space and time. In this method the steady state flow field is solved first, and then the unsteady fluctuations are solved. Steady and unsteady results are presented for a generic frigate shape. The parallel method is a necessity for ship airwake problems and MPI is used in the NLDE solver. Comparison of the parallel performance on various computers is also presented.**

**20010223 067**

# TRANSIENT RESPONSE ANALYSIS OF GIMBALLED TILTROTORS DURING ENGAGE AND DISENGAGE OPERATIONS

## Abstract

An analysis has been developed to predict transient aeroelastic response of gimballed tiltrotors during shipboard engage/disengage operations. The rotor blades are modeled with slender elastic beams undergoing flap bending, lag bending, elastic twist, and axial deflection attached to a gimballed rotor hub. The gimbal restraint is simulated using a conditional rotational spring. The rotor equations of motion are formulated using Hamilton's principle and spatially discretized using the finite element method. The discretized rotor equations of motion are integrated in time for a specified rotor speed run-up or run-down profile. Blade element theory is used to calculate quasi-steady loads in linear and nonlinear regimes. Studies for a 1/5<sup>th</sup>-size aeroelastically scaled tiltrotor model are conducted to validate the analysis and investigate transient response and loads of the gimballed rotor. Good correlation existed between the experimental data and the prediction of blade flap and lag moments in a hover condition. Blade bending moment and hub moment predictions indicated that gimbal restraint impacts could induce high transient loads on the rotor blades and hub. For  $\mu = 0.096$ , the peak flap and lag bending moment in the blade flexure are 130% and 310% above loads for a 1g hover condition.

## Introduction

Unique and often hazardous conditions are encountered when rotorcraft are operated from ship based platforms. One of the more troublesome rotorcraft/ship interface problems can occur during the engagement and disengagement of the rotor system while the aircraft is on the flight deck. Excessive aeroelastic flapping due to high wind over deck conditions can occur at low rotor speeds when the centrifugal stiffening is low. For articulated, the rotor blade can deflect several feet and contact the fuselage of the helicopter. For gimballed tiltrotors, the entire rotor assembly can tilt and contact the gimbal restraint, possibly resulting in high blade loads.

Excessive aeroelastic flapping of rotor blades at low rotational speeds, or "blade sailing", has been the subject of both analytical and experimental investigations over the past several years<sup>1-10</sup>. In the United Kingdom, Newman developed an analysis for the transient response of rotor blades during engagement and disengagement operations. A set of unique engage and disengage experimental tests were conducted by using scaled models in a wind tunnel<sup>1-5</sup>. The analytical model was applied to teetering and articulated rotors. At Penn State, Geyer and Smith also developed a transient aeroelastic response analysis for helicopters with articulated or hingeless rotor systems<sup>6-8</sup>. The finite element method was used to model the blade as an elastic beam undergoing deflections in flap bending and torsion. Blade element theory was used to calculate the quasi-steady or unsteady aerodynamic loads in linear and nonlinear regimes.

Present tiltrotor configurations, such as the V-22 Osprey, feature the use of a gimballed rotor system. A gimballed rotor has three or more blades attached to the hub without flap and lag hinges. The hub is attached to the rotor shaft by a universal joint, or gimbal. Other unique rotor characteristics include a gimbal spring and a gimbal restraint as shown in Figure 1. In addition, gimballed rotor blades are typically short and highly twisted.



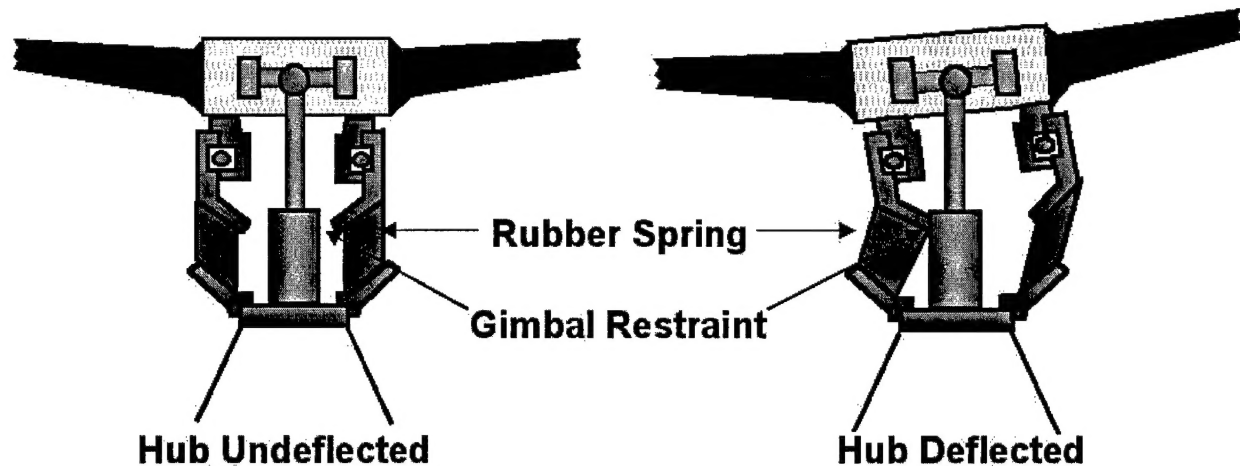


**Figure 1 - Gimballed Tiltrotor Hub Schematic**

Compared to articulated or hingeless rotor systems, the gimballed rotor has some unique structural and aerodynamic characteristics related to shipboard engagement and disengagement operations. The inflow distribution associated with the ship airwake on all blades contributes to gimbal flapping moments. The motion of all blades is coupled through the rotor hub. In addition, the highly twisted blades introduce significant structural flap-lag couplings and can result in high angles of attack at low rotor speeds.

An analytical model for steady-state aeroelastic response and stability of gimballed tiltrotors was developed in Ref. 11. The rotor model included coupled flap-lag bending modes and torsion degrees of freedom. The gimbal tilt was described by using the gimbal degrees of freedom,  $\beta_{GC}$  and  $\beta_{GS}$ , which are the pitch and roll of the rotor disk in nonrotating frame. In 1993, Nixon developed a comprehensive analysis for aeroelastic response and stability of tiltrotor with composite rotor blades<sup>12</sup>. Multi-blade rotor dynamics were studied in Ref. 13. A model was developed by using a set of nonlinear coupled flap-lag-torsion equations of motion for a two-bladed teetering rotor. The sensitivity of aeroelastic stability boundaries to structural and mechanical coupling was explored. For these analyses, the steady periodic response of the rotor could be obtained by considering the response of an equivalent single blade. For transient engagement and disengagement analyses, the motion of blades is non-periodic. In addition, gimbal restraint impacts make the individual blades respond differently and the inflow distribution on all blades contributes to gimbal motion. The entire multi-bladed gimballed rotor has to be modeled to analyze the transient response during engage and disengage operations.

## **Objectives**

The overall goal of this research is to systematically investigate the transient response of gimballed tiltrotors during shipboard engage/disengage operations by

1. Developing a comprehensive gimballed rotor model based on an elastic finite element model.
2. Determining transient gimbal motion, blade loads and hub loads.
3. Conducting parametric studies of rotor properties.

A separate goal of this research project is to develop computational techniques to determine the airwake environment around complex ship shapes. The results of this research are detailed in a report attached to this one. They can also be accessed online at <http://www.personal.psu.edu/faculty/l/n/lnl/frame2.html#papers>.

## Approach

To accurately predict the blade and hub loads associated with a gimbal restraint impact during engage and disengage operations; an elastic blade model is formulated. The following section presents the methodology and results from this analysis. A fixed rotor support was considered in the present research (i.e. rigid wing/pylon). The multi-bladed gimballed rotor is modeled as several slender elastic beams attached to a hub and undergoing flap bending, lag bending, elastic twist, and axial deflection. The blades are discretized into a number of beam elements using the finite element method. Each beam element consists of fifteen degrees of freedom<sup>18</sup>. The motion of gimbal is expressed by using two degrees of freedom in the rotating system. The partial differential equations governing the rotor motion are derived using Hamilton's Principle

$$\delta \Pi = \int_{t_1}^{t_2} (\delta T - \delta U - \delta W) dt = 0 \quad (1)$$

where  $\delta T$  is the variation of kinetic energy,  $\delta U$  is the variation of strain energy, and  $\delta W$  is the virtual work due to external forces. The contributions to these energy expressions may be summed as

$$\delta U = \sum_{m=1}^N \delta U_b^m + \delta U_{gs} + \delta U_{gr} + \delta U_{pl} \quad (2)$$

$$\delta T = \sum_{m=1}^N \delta T_b^m \quad (3)$$

$$\delta W = \sum_{m=1}^N \delta W_b^m \quad (4)$$

Where  $b$  refers to the blade,  $gs$  to the gimbal spring,  $gr$  to the gimbal restraint, and  $pl$  to the pitch link. Assuming isotropic elastic properties of blades, the variation of blade strain energy of the  $m^{\text{th}}$  blade can be expressed as

$$\delta U_b^m = \int_0^R \iint_A (E \varepsilon_{xx} \delta \varepsilon_{xx} + G \varepsilon_{x\eta} \delta \varepsilon_{x\eta} + G \varepsilon_{x\zeta} \delta \varepsilon_{x\zeta}) d\eta d\zeta dr \quad (5)$$

where  $\varepsilon_{xx}$  is the axial strain, and  $\varepsilon_{x\eta}$  and  $\varepsilon_{x\zeta}$  are engineering shear strains,  $E$  is the axial modulus of elasticity, and  $G$  is the shear modulus. The variation of gimbal spring strain energy is given by

$$\delta U_{gs} = K_\beta \beta_{GC} \delta \beta_{GC} + K_\phi \phi_{GS} \delta \phi_{GS} \quad (6)$$

The degrees of freedom in the rotating system ( $\beta$  and  $\phi$ ) are used to express the motion of gimbal. The transformation matrix is given by

$$\begin{Bmatrix} \beta_{GC} \\ \beta_{GS} \end{Bmatrix} = \begin{bmatrix} \cos \psi & -\sin \psi \\ \sin \psi & \cos \psi \end{bmatrix} \begin{Bmatrix} \beta \\ \phi \end{Bmatrix} \quad (7)$$

Where  $\psi$  is the azimuth angle of rotating frame,  $\beta$  and  $\phi$  are the gimbal tilt degrees of freedom in the rotating system. The gimbal degrees of freedom in nonrotating and rotating coordinate systems are shown in Figure 2.

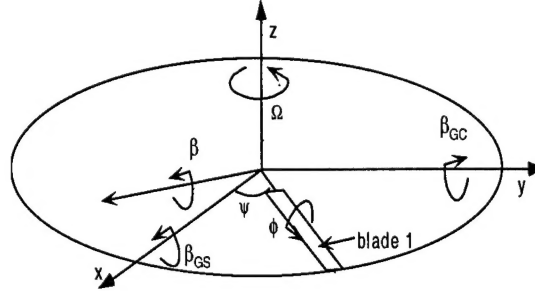


**Figure 2 - Gimbal Degrees of Freedom**

The variation of gimbal spring strain energy in the rotating system is much like Eqn. 6

$$\delta U_{gs} = K_{\beta} \beta \delta \beta + K_{\phi} \phi \delta \phi \quad (8)$$

This analysis models the gimbal restraint interaction with the rotor using a conditional rotational spring in nonrotating frame. The rotational spring stiffness is zero for tilt angles less than the gimbal restraint angle and large enough to restrict further tilt to less than  $0.1^{\circ}$  for tilt angles larger than the gimbal restraint angle. The variation of strain energy due to the gimbal restraint is expressed as

$$\delta U_{gr} = K_r (\beta_{\max} - \beta_r) \delta \beta_{\max} \quad (9)$$

The maximum tilt angle,  $\beta_{\max}$ , is given by

$$\beta_{\max} = (\beta \cos \psi - \phi \sin \psi) \cos \psi_{\max} + (\beta \sin \psi + \phi \cos \psi) \sin \psi_{\max} \quad (10)$$

Eqn. 9 can be expressed in the rotating system as:

$$\delta U_{gr} = K_r (A^2 \beta \delta \beta + B^2 \phi \delta \phi + AB \phi \delta \beta + AB \beta \delta \phi - A \beta_r \delta \beta - B \beta_r \delta \phi) \quad (11)$$

where

$$\begin{aligned} A &= \cos \psi \cos \psi_{\max} + \sin \psi \sin \psi_{\max} \\ B &= -\sin \psi \cos \psi_{\max} + \cos \psi \sin \psi_{\max} \end{aligned} \quad (12)$$

where  $\psi_{\max}$  is the azimuth angle where the maximum gimbal tilt angle is located and is given by

$$\psi_{\max} = \tan^{-1} \left( \frac{\beta \sin \psi + \phi \cos \psi}{\beta \cos \psi - \phi \sin \psi} \right) \quad (13)$$

The virtual work can be expressed as a summation of contributions from gravitational forces and aerodynamic forces

$$\delta W = \delta W_G + \delta W_{AF} \quad (14)$$

Gravitational forces are required in this analysis due to their effect on blade deflection over the low rotor speed regions. The work performed on the blade due to gravitational forces is expressed as

$$\delta W_G = - \int_0^R mg \delta w dr \quad (15)$$

where  $g$  is the acceleration due to gravity. The virtual work performed by the aerodynamic forces is given by

$$\delta W_{AF} = \int_0^R \left( L_v^A \delta v + L_w^A \delta w + M_{\phi}^A \delta \phi \right) dr \quad (16)$$

The unsteady aerodynamic model developed by Leishman and Beddoes is used for blade element airloads. Significant documentation on the development of this theory can be found in Refs. 15 and 16. The model is divided into three flow regions, attached flow unsteady aerodynamics, nonlinear aerodynamics (trailing edge separation), and dynamic stall. The unsteady attached flow model is based on an indicial response formulation and predicts both noncirculatory and circulatory airloads. A detailed description of the incorporation of Leishman and Beddoes' unsteady aerodynamic model into the present analysis is given in Ref. 6. During engage and disengage operations, the rotor speed,  $\Omega$ , is very low. The blades can experience large reverse flow regions and very high angles of attack compared to operation at normal rotor speed. The aerodynamic model used in this analysis must be modeled carefully for this situation. In order to simulate the aerodynamic loads at very high angles of attack ( $|\alpha| > 20^\circ$ ), a semi-empirical quasi-steady model was used to improve the quasi-steady aerodynamic force prediction<sup>17</sup>. For the angle of attack of section higher than  $20^\circ$ , the section lift, drag, and pitching moment coefficients are expressed as

$$\begin{aligned} c_l &= 1.15(1+M)^{0.6} \sin 2(\alpha - \alpha_{LO}) \\ c_d &= 1.05 + 0.5M - 1.04 \cos 2\alpha \\ c_m &= -0.55 \sin(\alpha - 10) \end{aligned} \quad (17)$$

where  $\alpha$  is the section angle of attack,  $\alpha_{LO}$  is the zero lift angle, and  $M$  is the Mach number. A quasi-steady aerodynamic model is used in this analysis. A linear gust model is used to simulate the airflow over a ship flight deck<sup>7</sup>. Detailed descriptions of the quasi-steady aerodynamic modeling and the shipboard aerodynamic environment are given in Ref 18 and Ref 6 respectively.

The variation of kinetic energy is given by

$$\delta T = \int_0^R \iint_A \rho_s \vec{V} \cdot \delta \vec{V} d\eta d\zeta dr \quad (18)$$

where  $\rho_s$  is the mass density of the blade and  $\vec{V}$  is the velocity vector at any point on the blade section. For engage and disengage operations, the rotating speed of the rotor is a function of time. The angular acceleration of the rotor,  $\dot{\Omega}$ , was also included in the kinetic energy.

An illustration of the blade finite element discretization is shown in Figure 3. Each of the flexible elements consists of fifteen degrees of freedom. These degrees of freedom are distributed over five element nodes, two external and three internal, which describe the elemental flap deflection ( $w, w'$ ), lag deflection ( $v, v'$ ), twist ( $\hat{\phi}$ ), and axial deflection ( $u$ ). Deformations within the element are described by shape functions. A more detailed description of these degrees of freedom and shape functions is given in Ref. 18. Note that the pitch bearing is located at the outboard part of the flexure.

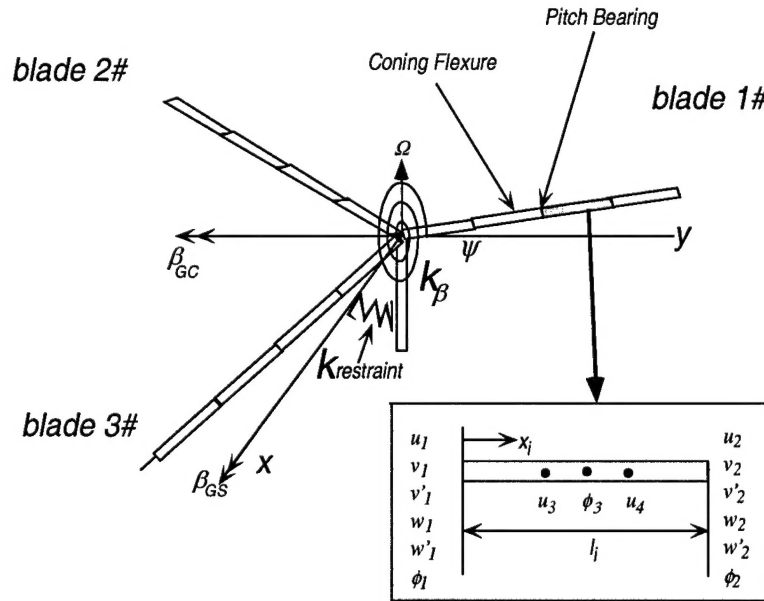


**Figure 3 - Finite Element Model of Gimbaled Rotor**

Figure 4 shows the global degrees of freedom for the gimbaled rotor. The first two degrees of freedom describes the gimbal tilt. The last degrees of freedom at the left-hand node of the second element of each blade describe the rotation of the pitch bearing. The second element is the flexure of the blade. For ten elements in each blade, there are 275 DOF with 30 elements for the entire rotor.

The energy expressions are spatially discretized by substituting the shape functions into the elemental virtual energy expressions. The resulting expressions are integrated in space using a six point Gaussian Quadrature method. The virtual energy expression for multi-bladed tiltrotor in terms of the elemental matrices and load vector becomes

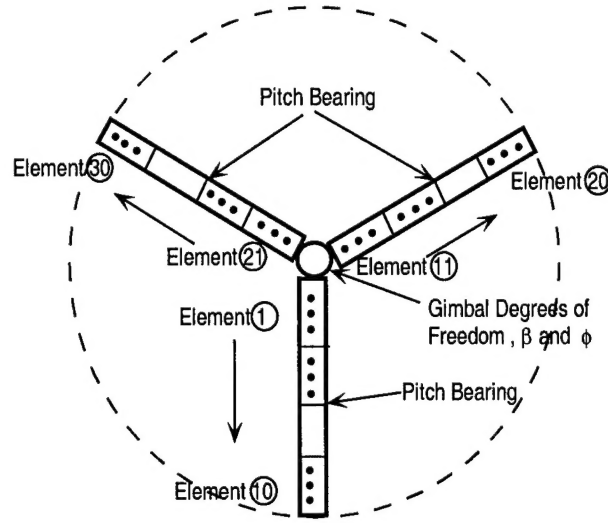


**Figure 4 – Global Degrees of Freedom and Finite Element Model Descriptions**

$$\delta \Pi = \int_{t_1}^{t_2} \sum_{m=1}^{N_b} \sum_{i=1}^N \delta \mathbf{q}_i^m T (\mathbf{M}_i^m \ddot{\mathbf{q}}_i^m + \mathbf{C}_i^m \dot{\mathbf{q}}_i^m + \mathbf{K}_i^m \mathbf{q}_i^m - \mathbf{F}_i^m) dt + \int_{t_1}^{t_2} \left( \begin{Bmatrix} \delta \beta \\ \delta \phi \end{Bmatrix}^T K_G \begin{Bmatrix} \beta \\ \phi \end{Bmatrix} + K_r (\beta_{\max} - \beta_r) \delta \beta_{\max} \right) dt \quad (19)$$

where  $K_G$  is the stiffness of matrix due to gimbal restraint and is expressed as

$$K_G = \begin{bmatrix} K_\beta & 0 \\ 0 & K_\phi \end{bmatrix} \quad (20)$$

$N_b$  is the number of blades for tiltrotor and  $N$  is the total number of spatial finite elements in one blade. The element nodal displacement vector,  $\mathbf{q}_i^m$ , is defined as

$$\mathbf{q}_i^m = \{u_1 \quad u_2 \quad u_3 \quad u_4 \quad v_1 \quad v'_1 \quad v_2 \quad v'_2 \quad w_1 \quad w'_1 \quad w_2 \quad w'_2 \quad \hat{\phi}_1 \quad \hat{\phi}_2 \quad \hat{\phi}_3\}^T \quad (21)$$

Where the subscript  $i$  refers to the  $i^{th}$  element of the  $m^{th}$  blade. For a gimbaled tiltrotor, the blade is fixed to the hub at the blade root. The hub is attached to the rotor shaft by a gimbal. The motion of the hub is expressed using two degrees of freedom in this analysis,  $\beta$  and  $\phi$ , which rotate with the rotor. The motion at the root of the blades can be determined by six degrees of freedom,  $u_1^m, v_1^m, v'_1{}^m, w_1^m, w'_1{}^m$  and  $\hat{\phi}_1^m$ . For the gimbaled rotor boundary conditions, the axial, vertical, and chordwise displacements response quantity,  $u$ ,  $v$ , and  $w$ , at each blade root are specified to be zero. The lag angle,  $v'$ , is specified to zero as well. Only the root slope,  $w'_1{}^m$  and twist,  $\hat{\phi}_1^m$ , are not restrained and can be expressed as a function of two gimbal degrees of freedom in the rotating frame,  $\beta$  and  $\phi$ .

$$w'_1{}^m = \beta \cos \psi_m + \phi \sin \psi_m \quad (22)$$

$$\hat{\phi}_1^m = -\beta \sin \psi_m + \phi \cos \psi_m \quad (23)$$

where the subscript 1 indicates the left-hand node of the first blade finite element. In this analysis, the node number order is defined from the root to the tip of the blade. The azimuth angle of each blade,  $\psi_m$ , in the rotating frame can be expressed as

$$\psi_m = \frac{2\pi}{N_b}(m-1) \quad (24)$$

Eqns. 22 and 23 are then substituted into Eqn. 19. The stiffness matrix, mass matrix, damping matrix and force vector for each element are then assembled to form their global counterparts. The variation of the total energy of the multi-bladed gimballed rotor system becomes

$$\delta \Pi = \int_{t_1}^{t_2} \delta \mathbf{q}^T (\mathbf{M}\ddot{\mathbf{q}} + \mathbf{C}\dot{\mathbf{q}} + \mathbf{K}\mathbf{q} - \mathbf{F}) dt \quad (25)$$

Finally, the discretized equation of rotor motion is obtained as

$$\mathbf{M}\ddot{\mathbf{q}} + \mathbf{C}\dot{\mathbf{q}} + \mathbf{K}\mathbf{q} = \mathbf{F} \quad (26)$$

where  $\mathbf{M}$ ,  $\mathbf{C}$ ,  $\mathbf{K}$ , and  $\mathbf{F}$  are mass matrix, damping matrix, stiffness matrix, and force vector of the *entire* rotor. The mass matrix, damping matrix and stiffness matrix include the linear structural, inertial and aerodynamic contributions. The force vector includes the constant structural, inertial and aerodynamic contributions as well as the nonlinear structural and aerodynamic contributions.

During gimbal restraint impacts, it is important to calculate blade and hub loads for design limits. The flap bending moment, lag bending moment, and twisting moment in the deformed coordinate system is defined by<sup>19</sup>

$$\begin{aligned} M_y^m &= EI_y (v'' \sin(\theta + \phi) - w'' \cos(\theta + \phi)) - EC_1 \phi'' \\ M_z^m &= -EAe_A \left( u' + \frac{v'^2}{2} + \frac{w'^2}{2} \right) - EB_2 \phi' \theta' + EI_z (v'' \cos(\theta + \phi) - w'' \sin(\theta + \phi)) \\ M_x^m &= GJ\phi' + EAK_A^2 (\theta + \phi)' \left( u' + \frac{v'^2}{2} + \frac{w'^2}{2} \right) + EB_1 \theta'^2 \phi' - EB_2 \theta' (v'' \cos \theta + w'' \sin \theta) \\ &\quad - [EC_1 \phi'' + EC_1 (w'' \cos \theta - v'' \sin \theta)]' \end{aligned} \quad (27)$$

where  $A$ ,  $Ae_A$ ,  $AK_A^2$ ,  $B_1$ ,  $B_2$ ,  $C_1$ , and  $C_2$  are section integrals. The pitch angle,  $\theta$ , is defined as

$$\theta = \theta_0 + \theta_{1c} \cos \psi_m + \theta_{1s} \sin \psi_m + \theta_{tw} (r - \frac{3}{4}) - k_p w_1^m \quad (28)$$



## Elastic Blade Model Results

### Validation

Experimental data for blade bending moments and twisting moments in a hover condition of a 1/5<sup>th</sup>-scale model of the V-22 gimballed rotor was used to validate the analysis. The test was conducted for a hover condition with varying collective pitch and zero cyclic pitch. The rotor speed is 875 RPM. The flap bending moment, lag bending moment, and twisting moment at six blade sections was measured. A comparison of these experimental results with the predictions of the present analysis is shown in Figure 8a and 8b. The flap and lag moments predicted by this analysis show good correlation with the experimental test data at moderate collective pitch. It should also be noted that no nonlinear aerodynamics was used for these calculations. Note that the element between section 0.11R and 0.15R represents the coning-flexure of the blade.

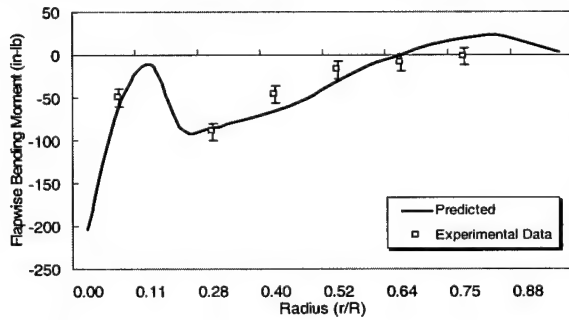


Figure 5a – Flap Moment Comparison

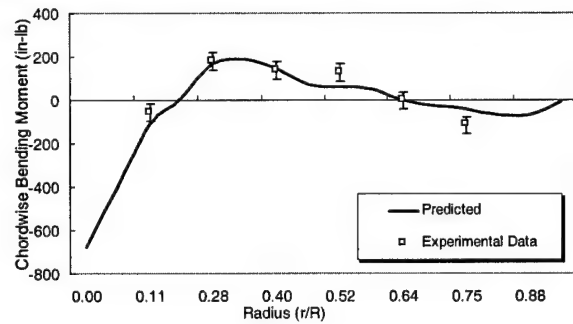


Figure 6a –Lag Moment Comparison

### Transient Response Analysis

The blade transient response is calculated by integrating the discretized rotor equations of motion for a specified rotor speed run-up profile. The rotor speed and azimuth run-up profiles are prescribed using experimental data. The experimentally determined rotor speed run-up profile (for the first 20 seconds) are expressed as

$$\Omega(t) = 3.08 \times 10^{-6} \times t^6 - 1.15 \times 10^{-4} \times t^5 + 1.79 \times 10^{-3} \times t^4 - 3.03 \times 10^{-3} \times t^2 - 4.92 \times 10^{-3} \times t^2 + 0.164 \quad (29)$$

In an effort to clearly understand engage/disengage behavior, an investigation was focused on the motions of the tiltrotor gimbal and bending moments of the blades. The tiltrotor operation was simulated for a starboard wind-over-deck of  $\mu = 0.075$ . A 25% upflow through the windward half of the rotor disk and a 25% downflow through the leeward half were simulated. The corresponding full-scale wind speed is equivalent to the 35 knots. The rotor collective pitch is set at  $0^\circ$  with zero cyclic control input. Figure 9 shows the time-history of transient response of gimbal tilt,  $\beta$  and  $\phi$ , and the maximum tilt,  $\beta_{max}$  for the run-up operation. The azimuth of rotor in graph is defined as the azimuth of rotor rotating and measured from downstream (forward flight) to span axis of the blade 1. The maximum tilt indicates the impacts between rotor and gimbal restraint during the run-up operation. The flap and lag bending moment time histories at section  $r/R=0.15$  (inboard section of flexure) in the blade 1 are shown in Figure 8. It can be seen that impacts between rotor and gimbal restraint cause substantial increase in blade bending moments.

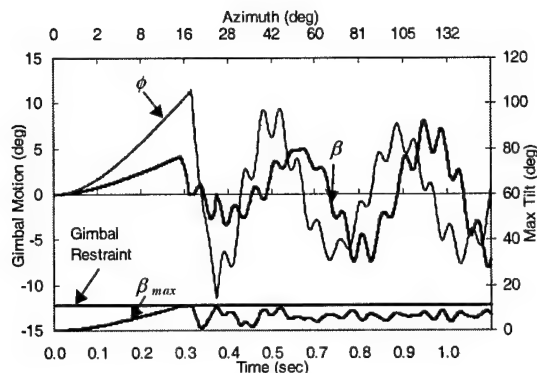


**Figure 7 –Transient Response**

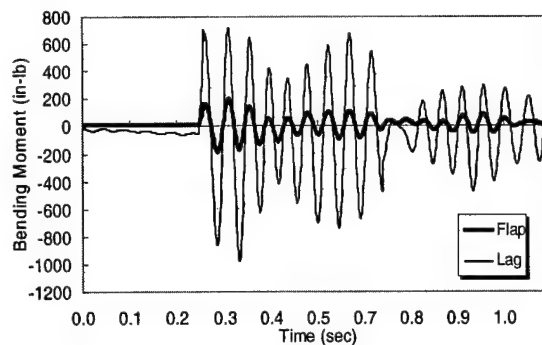


**Figure 8 –Bending Moment Response in Flexure**

### Wind speed effects

Blade moments were predicted for  $\mu = 0.075$  and  $\mu = 0.096$  starboard winds with a 25% upflow through the windward half of the rotor disk and a 25% downflow through the leeward half of the rotor for WRATS model rotor, which is corresponding to 35 and 50 knots for full-scale V-22 rotor. Rotor collective pitch is set at  $0^\circ$  with zero cyclic control input.

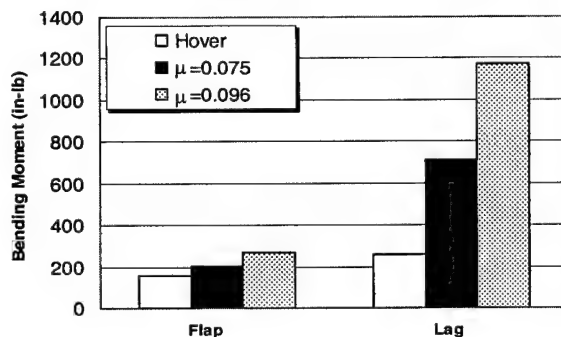


**Figure 9 – Comparison of Bending Moment at section 0.15R For Different Wind Speeds**

Figure 9 shows the comparison of blade flap and lag bending moment peak predictions at inboard section of the blade flexure (0.15R) during run-up operation. It shows that the bending moment peaks during run-up operation are much higher than in hover condition. The moment peaks appear when gimbal restraint impacts occur. For  $\mu = 0.075$ , the flap bending moment is 30% above loads for 1G hover condition; the lag bending moment is 130% above loads for hover condition. The flap bending moment peak for  $\mu = 0.096$  is 1.3 times bending moment peak for  $\mu = 0.075$ . The lag bending moment peak for the higher wind speed is 1.8 times moment peak for lower wind speed.

## **Summary and Conclusions**

An analysis has been developed to predict transient aeroelastic gimbal tiltrotor response during rotor engage/disengage sequences. The multi-blade gimbaled rotor is modeled as several slender elastic beams attached to a hub, which undergo flap bending, lag bending, elastic twist, and axial deflections. The gimbal restraint is simulated using a conditional rotational spring.

Gimbal motion is expressed by using two degrees of freedom in the rotating frame. The rotor equations of motion were formulated using Hamilton's principle and spatially discretized using the finite element method. The discretized rotor equations of motion were integrated in modal space for a specified rotor speed run-up or run-down profile. Blade element theory was used to calculate quasi-steady loads in linear and nonlinear regimes. Parametric studies for a 1/5<sup>th</sup> size aeroelastically scaled V-22 tiltrotor model were conducted to investigate the transient response characteristics and effects of wind speed and blade flexure stiffness on transient rotor motion and blade and hub loads. Predictions showed that for  $\mu = 0.075$ , the flap bending moment is 30% above loads for 1g hover condition; the lag bending moment is 130% above loads for hover condition.

## References

1. Hurst, D.W. and Newman, S.J., "Wind Tunnel Measurements of Ship Induced Turbulence and the Prediction of Helicopter Rotor Blade Response," *Proceedings of the Eleventh European Rotorcraft Forum*, Paper No. 99, London, England, Sept. 1985.
2. Newman, S.J., "A Theoretical Model for the Predicting the Blade Sailing Behaviour of a Semi-Rigid Rotor Helicopter," *Vertica*, Vol. 14, No. 4, 1990.
3. Newman, S.J., "The Application of a Theoretical Blade Sailing Model to Predict the Behaviour of Articulated Rotor Helicopters," *The Aeronautical Journal of the Royal Aeronautical Society*, June/July 1992.
4. Newman, S.J., "The Problems of Rotor Engagement and Disengagement of a Shipborne Helicopter," *Journal of Naval Sciences*, Vol. 20, No. 1, 1994.
5. Newman, S.J., "The Verification of a Theoretical Helicopter Rotor Blade Sailing Method by Means of Windtunnel Testing," *The Aeronautical Journal of the Royal Aeronautical Society*, Feb. 1995.
6. Geyer, W.P., "Aeroelastic Analysis of Transient Blade Dynamics During Shipboard Engage/Disengage Operations," M.S. Thesis, Department of Aerospace Engineering, The Pennsylvania State University, University Park, PA, Aug. 1995.
7. Geyer, W.P., and Smith, E.C., "Aeroelastic Analysis of Transient Blade Dynamics During Shipboard Engage/Disengage Operations," *Proceedings of the 2nd International Aeromechanics Specialists' Conference* (Bridgeport, CT), Oct. 1995.
8. Geyer, W.P., Smith E.C., and Keller, J., "Validation and Application of a Transient Aeroelastic Analysis for Shipboard Engage/Disengage Operations," *Proceedings of the 52nd Forum of the American Helicopter Society* (Washington, D.C.), June 1996.
9. Keller, J.A., and Smith E.C., "Experimental and Theoretical Correlation of Analysis for Helicopter Rotor Blade/Droop Stop Impacts" *Proceedings of the 38<sup>th</sup> AIAA/ASME/ASCE/AHS/ASC Structures, Structural Dynamics, and Materials Conference* (Kissimmee, FL), Apr. 1997.
10. Keller, J.A., "An Experimental and Theoretical Correlation of An Analysis for Helicopter Rotor Blade and Droop Stop Impacts," M.S. Thesis, Department of Aerospace Engineering, The Pennsylvania State University, University Park, PA, Dec. 1997.

11. Johnson, W., "Analytical Model for Tilting Proprotor Aircraft Dynamics, Including Blade Torsion and Coupled Bending Modes, and Conversion Mode Operation," NASA TM X-62369, Aug. 1974.
12. Nixon, M.W., "Aeroelastic Response and Stability of Tiltrotors with Elastically-Coupled Composite Rotor Blades," Ph.D. Thesis, Department of Aerospace Engineering, University of Maryland, College Park, MD, 1993.
13. Kawakami, N., "Dynamics of an Elastic Seesaw Rotor," *Journal of Aircraft*, Vol. 14, No. 3, 1977.
14. Shamie, J., and Friedmann, P., "Aeroelastic Stability of Complete Rotors with Application to a Teetering Rotor in Forward Flight," *Journal of Sound and Vibration*, Vol. 53, No. 4, 1977.
15. Leishman, J.G., and Beddoes, T.S., "A Generalised Model for Airfoil Unsteady Aerodynamic Behaviour and Dynamic Stall Using the Indical Method," *Proceedings of the 42nd Forum of the American Helicopter Society* (Washington, D.C.), June 1986.
16. Leishman, J.G., and Beddoes, T.S., "A Semi-Empirical Model for Dynamic Stall," *Journal of the American Helicopter Society*, Vol. 9, July 1989.
17. Prouty, R.W., Helicopter Performance, Stability, and Control, Robert E. Krieger Publishing Company, Malabar, Florida, 1990.
18. Bir, G., and Chopra I., "Theory Manual of UMARC" University of Maryland, UM-AERO, 94-18, College Park, MD, July 1994.
19. Hodges D.H., and Dowell E.H., "Nonlinear Equations of Motion for the Elastic Bending and Torsion of Twisted Nonuniform Rotor Blades," NASA TN D-7818, 1994.
20. Johnson, W., "An Assessment of the Capability to Calculate Tilting Proprotor Aircraft Performance, Loads, and," NASA Technical Paper 22291, 1974.
21. Johnson, W., "Analytical Modeling Requirements for Tilting Proprotor Aircraft Dynamics," NASA TN D-8013, July 1975.
22. Srinivas, V., "Aeroelastic Analysis of Advanced Tiltrotor Aircraft," Ph.D. Thesis, Department of Aerospace Engineering, University of Maryland, College Park, MD, 1995.

# Higher Order Accurate Solutions of Ship Airwake Flow Fields Using Parallel Computer

Jingmei Liu \*, Lyle N. Long<sup>†</sup> and Anirudh Modi<sup>‡</sup>  
Department of Aerospace Engineering  
The Pennsylvania State University  
University Park, PA 16802  
lnl@psu.edu

## Abstract

This paper presents a new method for simulating ship airwake flow fields. These flows are inherently unsteady, and very difficult to predict. The method presented (NLDE) is fourth-order accurate in space and time. In this method we first solve for the steady state flow field, then we solve for the unsteady fluctuations. Steady and unsteady results are presented for a generic frigate shape. The parallel method is a necessity for ship air wake problems and MPI is used in the NLDE solver. The parallel performance on various computers is compared also.

## Introduction

Sharp-edged box-like ship super-structures create numerous aerodynamic and fluid dynamic problems. Unsteady separated flow from sharp edges (and excessive ship motions) make landing helicopters on ships a very hazardous operation. In addition, the strong unsteady flows can cause severe rotor blade deformations. There have been numerous incidences where the helicopter blades have actually impacted the helicopter fuselage, which is called a "tunnel strike".<sup>9,10</sup> In order to avoid this and other engage/disengage problems, determining safe operating envelopes is very costly and time consuming. On the other hand, many numerical simulation attempts of this flow field have not been successful due to the inherently unsteady nature of flow and the low-speed character of the flow (which may cause numerical stiffness).

Research on ship airwakes has been conducted using several different approaches.<sup>5</sup> One of the sources of relevant research is building aerodynamics which shows the general features of flow about blunt bodies of different

aspect ratios. The simplest model of a ship, admittedly rather crude, is a sharp edged blunt body. The super-structure of most modern ships is very complicated, including towers, antennae, radar dishes, exhaust stacks, etc. The flow around these obstacles is very difficult to predict.

Geometrically precise studies are needed and have been done in wind tunnels.<sup>7,8,17</sup> There have also been full scale tests performed by the US Navy,<sup>11</sup> which gives some important information on real ship airwakes. Of course it is difficult to perform very controlled experiments on real ships. It is also difficult to measure the flow field accurately in the harsh ocean environment and in the presence of the strong electromagnetic fields on most ships.

Most wind tunnel tests include measurements made in the wake of a model ship exposed to a uniform velocity profile and almost zero turbulence level. One more realistic test was conducted at NASA Ames in the "Ship-board Simulator" with a neutrally buoyant atmospheric boundary layer.<sup>7</sup>

Another reference for simulations is that by NRC-CNRC.<sup>22</sup> A wind tunnel investigation of the characteristics of the airwake behind a model of a generic frigate was conducted. The wind tunnel simulation incorporated a correctly-scaled atmospheric boundary layer. Measurements of streamwise and vertical components of airwake velocity were made. Time average, standard deviations, spectral densities and time correlations are presented for both velocity components for various position in the airwake.

The wind tunnel tests have to suitably scale the environment and structure to model size, make the appropriate measurements in the wake of the model and then rescale the results back to full size. All these experimental tests are crucial for validating numerical models. Wind tunnel tests can be quite costly, but flow measurements on real Naval ships are very difficult and costly to obtain.

Figs. 1 and 2 show a frigate and an LHA, respec-

\*Research Associate

†Professor

‡Master Candidate

<sup>0</sup>Presented at the American Helicopter Society 54th Annual Forum, Washington, DC, May 20-22, 1998. Copyright ©1998 by the American helicopter Society, Inc. All right reserved.

tively. These are very different ships, and their airwakes are very different also. The frigates typically carry one or two SH-2G Seasprites or SH-60B Seahawks. On the frigate we are mainly interested in studying the hangar deck area (aft portion of the ship), and the separated flow that effects this region. On the LHA, helicopters can land on many different locations on the deck, and each of these can experience quite different flow fields. The LHA's can carry 9 CH-53D Sea Stallions or 12 CH-46D Sea Knight helicopters, and 6 AV-8B Harriers. The forward portion of the deck is primarily influenced by the separated flow off the deck edge. Very strong vortex sheets emanate from these edges. One of the authors (Long) spent three days on an LHA (U.S.S. Saipan) and helped Kurt Long measure ship airwakes. We found in some cases the flow velocity ranged from 40 knots 12 feet off the deck to zero velocity 3 feet off the deck. In the mid-section of the ship the very large island has a strong effect on the flow and tunnels the flow tangential to the island.



Figure 1: Oliver Hazard Perry Class Guided Missile Frigate (length=445 feet, beam=45 feet)

The need for numerical simulations comes from the very high cost of determining the safe operating envelopes for helicopters in a ship environment (and the huge testing backlog). It would be very useful to have numerical methods that could accurately simulate ship airwakes. There have been other attempts at numerically simulating ship airwakes. The airwake about a DD-963 ship configuration was simulated using a steady-state flow solver based on the 3D multi-zone, thin-layer Navier-Stokes method.<sup>19</sup> A US navy destroyer, DDG51 was chosen to validate an unsteady inviscid solver with an unstructured grid and low-order method.<sup>12,13</sup> No method to-date has been entirely satisfactory for predicting these flow fields.

## Flow Nature of Ship Airwake



Figure 2: Tarawa Class LHA (length = 820 feet, beam = 132 feet)

## Simulation

From previous studies, it has been shown that the key features of ship airwakes are (1) a low Mach number (about 0.05), (2) inherently unsteady flow, and (3) large regions of separated flow. The large separated regions from superstructure sharp edges are quite difficult to capture accurately. In addition, the wind conditions over rough seas have to be considered, such as, the atmospheric turbulent boundary layer and the effect of the wind/ship speed ratio on the turbulence intensity. When this ratio is increased, the turbulence intensity will decrease and its spectrum will shift to a high value in the streamwise direction. The wind direction can vary a great deal, since the air flow can impact the ship at any yaw angle (even 180 degrees). The complex ship geometry makes unstructured grid solvers and parallel computers very attractive. In this paper, preliminary attempts at high order accurate ship airwake predictions have been made by solving a steady flow field with a well-developed CFD method (CFL3D<sup>18</sup>) and a perturbation field with a high-order method. The result is high-order-accurate 3D simulations. We will only show structured grid results herein, but we are also pursuing higher-order accurate unstructured solvers (e.g. based on PUMA<sup>1</sup>).

## Nonlinear Disturbance Equations (NLDE)

The methodology used here is based on the nonlinear disturbance equations, which is a newly developed numerical method.<sup>14</sup> The general Navier-Stokes equations in a Cartesian coordinate system are:

$$\frac{\partial q}{\partial t} + \frac{\partial F}{\partial x} + \frac{\partial G}{\partial y} + \frac{\partial H}{\partial z} = \frac{\partial R}{\partial x} + \frac{\partial S}{\partial y} + \frac{\partial E}{\partial z} \quad (1)$$

where  $F$ ,  $G$ , and  $H$  are the inviscid terms and  $R$ ,  $S$ ,  $E$  are the viscous terms. The results presented here will all be inviscid. The flow field is then split into a mean and a fluctuating part:

$$q = q_o + q' \quad (2)$$

where

$$q = \begin{Bmatrix} \rho \\ \rho u \\ \rho v \\ \rho w \\ e \end{Bmatrix} \quad (3)$$

and

$$q_o = \lim_{T \rightarrow \infty} \frac{1}{T} \int_{t_o}^{t_o+T} q(t) dt \quad (4)$$

Substitution of equation (2) into (1) and rearranging results in the nonlinear disturbance equations (NLDE):

$$\frac{\partial q'}{\partial t} + \frac{\partial F'}{\partial x} + \frac{\partial G'}{\partial y} + \frac{\partial H'}{\partial z} = Q \quad (5)$$

Where

$$q' = \begin{Bmatrix} \rho' \\ \rho_o u' + \rho' u_o + \rho' u' \\ \rho_o v' + \rho' v_o + \rho' v' \\ \rho_o w' + \rho' w_o + \rho' w' \\ e' \end{Bmatrix} \quad (6)$$

On the left hand side of the NLDE are terms related to the perturbation properties and the cross terms (linear and nonlinear), whereas the right hand side contains strictly mean flow terms.

The convective fluxes involving the perturbation quantities  $F'$ ,  $G'$  and  $H'$  are given as

$$F' = \begin{Bmatrix} \rho_o u' + \rho' u_o + \rho' u' \\ \rho' u_o^2 + 2\rho_o u_o u' + p' \\ + 2\rho' u' u_o + (\rho_o + \rho') u' u' \\ \rho_o u_o v' + \rho_o v_o u' + \rho' u_o v_o \\ + \rho' v' u_o + \rho' u' v_o + (\rho_o + \rho') u' v' \\ \rho_o u_o w' + \rho_o w_o u' + \rho' u_o w_o \\ + \rho' w' u_o + \rho' u' w_o + (\rho_o + \rho') u' w' \\ u'(e_o + p_o) + (u_o + u')(e' + p') \end{Bmatrix} \quad (7)$$

$$G' = \begin{Bmatrix} \rho_o v' + \rho' v_o + \rho' v' \\ \rho_o v_o u' + \rho_o u_o v' + \rho' u_o v_o \\ + \rho' v' u_o + \rho' u' v_o + (\rho_o + \rho') u' v' \\ \rho' v_o^2 + 2\rho_o v_o v' + p' \\ + 2\rho' v' v_o + (\rho_o + \rho') v' v' \\ \rho_o v_o w' + \rho_o w_o v' + \rho' v_o w_o \\ + \rho' w' v_o + \rho' v' w_o + (\rho_o + \rho') v' w' \\ v'(e_o + p_o) + (v_o + v')(e' + p') \end{Bmatrix} \quad (8)$$

$$H' = \begin{Bmatrix} \rho_o w' + \rho' w_o + \rho' w' \\ \rho_o w_o u' + \rho_o u_o w' + \rho' u_o w_o \\ + \rho' w' u_o + \rho' u' w_o + (\rho_o + \rho') u' w' \\ \rho_o w_o v' + \rho_o v_o w' + \rho' w_o v_o \\ + \rho' w' v_o + \rho' v' w_o + (\rho_o + \rho') v' w' \\ \rho' w_o^2 + 2\rho_o w_o w' + p' \\ + 2\rho' w' w_o + (\rho_o + \rho') w' w' \\ w'(e_o + p_o) + (w_o + w')(e' + p') \end{Bmatrix} \quad (9)$$

The mean flow source term  $Q$  is time independent:

$$Q = - \left( \frac{\partial F_o}{\partial x} + \frac{\partial G_o}{\partial y} + \frac{\partial H_o}{\partial z} \right) + \frac{\partial R_o}{\partial x} + \frac{\partial S_o}{\partial y} + \frac{\partial E_o}{\partial z} \quad (10)$$

If the NLDE is time averaged, it becomes the Reynolds-averaged Navier-Stokes equation, where the Reynold's stresses are on the left hand side. Thus, for a laminar flow  $Q = 0$ .

We seek a solution of the perturbation variables  $q'$  with a known mean flow field which can be obtained from existing well-developed CFD codes (e.g. CFL3D,<sup>18</sup> INS3D, OVERFLOW, PUMA,<sup>1</sup> ...) for steady flow. This methodology allows us to use the most effective algorithms for the steady and unsteady portions of field, respectively. It also minimizes round-off error since we are only computing perturbations. We can even use different grids for the steady and unsteady solution. More discussion on this new method is in the reference.<sup>14</sup>

## Characteristic Boundary Conditions for NLDE

The boundary conditions for the NLDE are developed by applying Thompson's characteristic method<sup>21</sup> to the nonlinear disturbance equations. Instead of using the conservative form of the equations, the boundary conditions are derived based on the nonconservative form:

$$\frac{\partial \rho}{\partial t} + \rho \frac{\partial u_j}{\partial x_j} + u_j \frac{\partial \rho}{\partial x_j} = 0 \quad (11)$$



$$\frac{\partial p}{\partial t} + \gamma p \frac{\partial u_j}{\partial x_j} + u_j \frac{\partial p}{\partial x_j} - VIS_p = 0 \quad (12)$$

$$\rho \frac{\partial u_i}{\partial t} + \rho u_j \frac{\partial u_i}{\partial x_j} + \frac{\partial p}{\partial x_i} - VIS_{vel} = 0 \quad (13)$$

Here  $VIS_p$  and  $VIS_{vel}$  are viscous terms. Substitution of equation (2) into (11) - (13) and rearranging the results gives the boundary conditions in nonlinear perturbation form:

$$\begin{aligned} \frac{\partial p'}{\partial t} + (\rho_0 + \rho') \frac{\partial u_j'}{\partial x_j} + (u_{0j} + u_j') \frac{\partial p'}{\partial x_j} = \\ -(\rho' \frac{\partial u_{0j}}{\partial x_j} + u_j' \frac{\partial \rho_0}{\partial x_j}) - (\rho_0 \frac{\partial u_{0j}}{\partial x_j} + u_{0j} \frac{\partial \rho_0}{\partial x_j}) \end{aligned} \quad (14)$$

$$\begin{aligned} \frac{\partial p'}{\partial t} + \gamma(p_0 + p') \frac{\partial u_j'}{\partial x_j} + (u_{0j} + u_j') \frac{\partial p'}{\partial x_j} = \\ -(\gamma p' \frac{\partial u_{0j}}{\partial x_j} + u_j' \frac{\partial p_0}{\partial x_j}) - (\gamma p_0 \frac{\partial u_{0j}}{\partial x_j} + u_{0j} \frac{\partial p_0}{\partial x_j}) \\ + VIS_p \end{aligned} \quad (15)$$

$$\begin{aligned} \frac{\partial u_i'}{\partial t} + (u_{0j} + u_j') \frac{\partial u_i'}{\partial x_j} + \frac{1}{\rho_0 + \rho'} \frac{\partial p'}{\partial x_i} = \\ -(u_j' \frac{\partial u_{0i}}{\partial x_j} + \frac{1}{\rho_0 + \rho'} \frac{\partial p_0}{\partial x_i}) - u_{0j} \frac{\partial u_{0i}}{\partial x_j} \\ + VIS_{vel} \end{aligned} \quad (16)$$

Here we apply a characteristic analysis to the perturbation variables and move the mean flow terms to the right hand side, which is different than the approach employed by others. Now considering a boundary located at  $x = x_0$  and using the characteristic analysis<sup>21</sup> to modify the hyperbolic terms of Eqs. (14) - (15) corresponding to waves propagating in the  $x$  direction, we can recast this system as:

$$\begin{aligned} \frac{\partial p'}{\partial t} + \frac{1}{c^2} [L_2 + \frac{1}{2}(L_1 + L_5)] + (\rho_0 + \rho') (\frac{\partial v'}{\partial y} + \frac{\partial w'}{\partial z}) \\ + (v_0 + v') \frac{\partial p'}{\partial y} + (w_0 + w') \frac{\partial p'}{\partial z} = -[\rho' (\frac{\partial u_0}{\partial x} + \frac{\partial v_0}{\partial y} + \\ \frac{\partial w_0}{\partial z}) + (u' \frac{\partial \rho_0}{\partial x} + v' \frac{\partial \rho_0}{\partial y} + w' \frac{\partial \rho_0}{\partial z}) - [\rho_0 (\frac{\partial u_0}{\partial x} + \\ \frac{\partial v_0}{\partial y} + \frac{\partial w_0}{\partial z}) + (u_0 \frac{\partial \rho_0}{\partial x} + v_0 \frac{\partial \rho_0}{\partial y} + w_0 \frac{\partial \rho_0}{\partial z})] \end{aligned} \quad (17)$$

$$\frac{\partial p'}{\partial t} + \frac{1}{2}(L_1 + L_5) + \gamma(p_0 + p') (\frac{\partial v'}{\partial y} + \frac{\partial w'}{\partial z}) +$$

$$\begin{aligned} (v_0 + v') \frac{\partial p'}{\partial y} + (w_0 + w') \frac{\partial p'}{\partial z} = -[\gamma p' (\frac{\partial u_0}{\partial x} + \\ \frac{\partial v_0}{\partial y} + \frac{\partial w_0}{\partial z}) + (u' \frac{\partial p_0}{\partial x} + v' \frac{\partial p_0}{\partial y} + w' \frac{\partial p_0}{\partial z})] \\ -[\gamma p_0 (\frac{\partial u_0}{\partial x} + \frac{\partial v_0}{\partial y} + \frac{\partial w_0}{\partial z}) + (u_0 \frac{\partial p_0}{\partial x} + \\ v_0 \frac{\partial p_0}{\partial y} + w_0 \frac{\partial p_0}{\partial z})] + VIS_p \end{aligned} \quad (18)$$

$$\begin{aligned} \frac{\partial u'}{\partial t} + \frac{1}{2(\rho_0 + \rho')c} (L_5 - L_1) + (v_0 + v') \frac{\partial u'}{\partial y} + \\ (w_0 + w') \frac{\partial u'}{\partial z} = -[u' \frac{\partial u_0}{\partial x} + v' \frac{\partial u_0}{\partial y} + w' \frac{\partial u_0}{\partial z}] \\ -[(u_0 \frac{\partial u_0}{\partial x} + v_0 \frac{\partial u_0}{\partial y} + w_0 \frac{\partial u_0}{\partial z}) + \frac{1}{\rho_0 + \rho'} \frac{\partial p_0}{\partial x} \\ + VIS_u] \end{aligned} \quad (19)$$

$$\begin{aligned} \frac{\partial v'}{\partial t} + L_3 + (v_0 + v') \frac{\partial v'}{\partial y} + (w_0 + w') \frac{\partial v'}{\partial z} + \\ \frac{1}{\rho_0 + \rho'} \frac{\partial p'}{\partial y} = -[u' \frac{\partial v_0}{\partial x} + v' \frac{\partial v_0}{\partial y} + w' \frac{\partial v_0}{\partial z}] \\ -[(u_0 \frac{\partial v_0}{\partial x} + v_0 \frac{\partial v_0}{\partial y} + w_0 \frac{\partial v_0}{\partial z}) + \frac{1}{\rho_0 + \rho'} \frac{\partial p_0}{\partial y} \\ + VIS_v] \end{aligned} \quad (20)$$

$$\begin{aligned} \frac{\partial w'}{\partial t} + L_4 + (v_0 + v') \frac{\partial w'}{\partial y} + (w_0 + w') \frac{\partial w'}{\partial z} + \\ \frac{1}{\rho_0 + \rho'} \frac{\partial p'}{\partial z} = -[u' \frac{\partial w_0}{\partial x} + v' \frac{\partial w_0}{\partial y} + w' \frac{\partial w_0}{\partial z}] \\ -[(u_0 \frac{\partial w_0}{\partial x} + v_0 \frac{\partial w_0}{\partial y} + w_0 \frac{\partial w_0}{\partial z}) + \frac{1}{\rho_0 + \rho'} \frac{\partial p_0}{\partial z} \\ + VIS_w] \end{aligned} \quad (21)$$

where the  $L_i$ 's are the amplitudes of characteristic waves associated with each characteristic velocity  $\lambda_i$ . These velocities are given by:

$$\lambda_1 = (u_0 + u') - c \quad (22)$$

$$\lambda_2 = \lambda_3 = \lambda_4 = u_0 + u' \quad (23)$$

$$\lambda_5 = (u_0 + u') + c \quad (24)$$

where  $c$  is the speed of sound:

$$c^2 = \gamma \frac{p_0 + p'}{\rho_0 + \rho'} \quad (25)$$

$\lambda_1$  and  $\lambda_5$  are the speed of acoustic waves moving in the negative and positive  $x$  direction;  $\lambda_2$  is the convection

velocity (the speed at which entropy waves will travel) while  $\lambda_3$  and  $\lambda_4$  are the velocities at which  $v$  and  $w$  are advected in the  $x$  direction. The  $L_i$ 's are given by:

$$L_1 = \lambda_1 \left[ \frac{\partial p'}{\partial x} - (\rho_0 + \rho') c \frac{\partial u'}{\partial x} \right] \quad (26)$$

$$L_2 = \lambda_2 \left( c^2 \frac{\partial \rho'}{\partial x} - \frac{\partial p'}{\partial x} \right) \quad (27)$$

$$L_3 = \lambda_3 \frac{\partial v'}{\partial x} \quad (28)$$

$$L_4 = \lambda_4 \frac{\partial w'}{\partial x} \quad (29)$$

$$L_5 = \lambda_5 \left[ \frac{\partial p'}{\partial x} + (\rho_0 + \rho') c \frac{\partial u'}{\partial x} \right] \quad (30)$$

We have shown here the characteristic boundary conditions in the  $x$  direction. The equations for the  $y$  and  $z$  direction are derived in a similar manner. For edges and corners in three dimensional situations a simple extension is used by combining the equations for the various directions into one approximate equation.

This type of boundary condition treatment also allows one to easily introduce a disturbance at the incoming boundary by deriving an expression for one of the incoming characteristics with a source term. Atmospheric boundary layer conditions can be incorporated in this manner at incoming boundaries. At the outflow boundaries, the boundary conditions are essentially non-reflecting. The ship superstructure and ocean surface are both treated as hard wall boundary conditions.

## Numerical Method and Parallel Methodology

The NLDE are cast in a generalized coordinate system and solved numerically using a finite difference based scheme. The discretized equations are solved in a time accurate manner by taking advantage of computational aeroacoustics (CAA) methods. The spatial flux derivatives are calculated using seven point stencils of the fourth order optimized Dispersion Relation Preserving (DRP) scheme of Tam and Webb.<sup>20</sup> The time integration is a fourth order accurate Runge-Kutta method.

Efficient computing performance is achieved by using a three dimensional domain decomposition strategy. The code is written in Fortran 77 plus Message Passing Interface (MPI)<sup>15</sup> and is scalable in three dimensions. As mentioned early, the ship geometry is very complicated, even for a generic frigate test model. This makes multi-block grid simulations and domain decomposition very difficult. In order to make the code scalable and flexible, a three dimensional single-block grid is used. The whole

computational domain is divided into many three dimensional zones. The grid points are evenly distributed across each processor.

The NLDE solver is implemented portably on parallel computers, such as, the IBM SP2 (e.g. Penn State, Npaci, MHPCC), SGI Power Challenge and Pentium II Cluster. A comparison of code performance for the ship airwake run on various machines is shown in Fig. 3. While a 24-processor IBM SP2 is 8.4 times faster than 8 Pentium II's networked together, the SP2 costs roughly 14 times more than the PC cluster. Fig. 4 gives the wall clock time for a ship air wake case with 1.86 million grid points using various number of processors. A 64-processor SP2 is roughly 2.6 times faster than a 16-processor SP2 (when problem size is kept fixed).

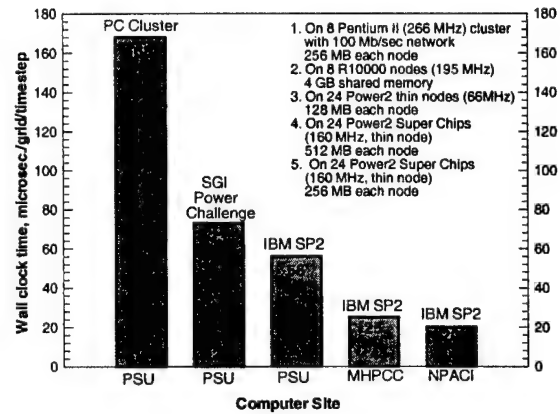


Figure 3: Timings for a ship air wake case on several parallel computers

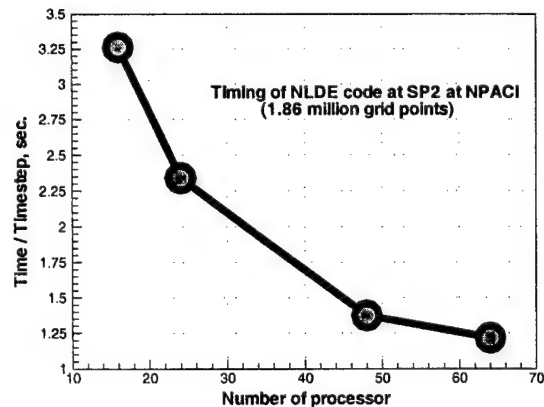


Figure 4: Timings for a ship air wake case on SP2

## Results and Discussions

In the helicopter/ship interface problem, the most important data for coupling the airwake solution to the dynamics analysis of the main rotor blades of helicopter are the mean flow field, the intensity of flow perturbations, and its dominant frequencies. Such an approach is presented in this paper. So far we have been concentrating on two types of ships: (1) frigates with helicopter landing pads on the deck behind the hangar and (2) aircraft carriers and LHA's with several helicopter landing spots on the deck around the control tower. The airwake influences on the helicopter are quite different in these two cases. For frigates the flow separation area behind the hangar cube has a strong effect on a landing helicopter, while on LHA's the deck leading edge vortex and separation are the key flow phenomena. Fig. 5 is some of the experimental data obtain by one of the authors (L. Long) with K. Long (PAX River) on the U.S.S Saipan (an LHA). It shows the flow velocity at different heights from the deck in the center plane. This was obtained from a cup anemometer and only includes the effects of velocity in the longitudinal and normal (to deck) directions. The wind was at 36 knots and had a 30 degree yaw angle. These data will eventually be used to validate numerical results for the LHA case.

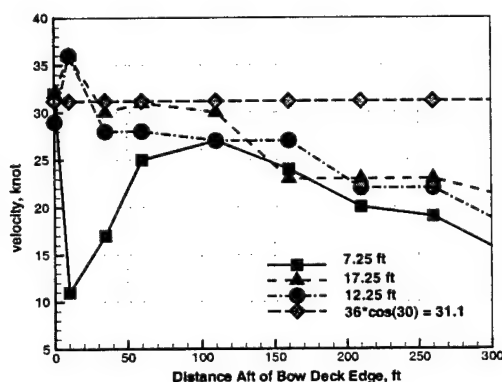


Figure 5: Field measurement of LHA

In this paper some preliminary simulations have been done for a generic ship shape (TTCP ship). In fact, this is a generic frigate model and it is shown in Fig. 6 in a computational mesh. It is 240 feet long, 45 feet wide and 55 feet high. It was chosen because there will be some experimental investigations using the same configuration. It is acknowledged that the ship superstructure does not resemble a typical frigate superstructure in detail. However, from an aerodynamic point of view the airwake should still be representative of that for an actual frigate since this study is concerned with the macro-

scopic flow properties and large scale phenomena in the hangar wake.

Special attention is given to the helicopter landing area which is the square, aft section of the ship. There is a 20 feet drop down to the landing deck from the hangar structure, which will lead to vortex shedding over the deck causing landing approach hazards.

The computational grid for this problem is  $201 \times 109 \times 85$  which results in a grid resolution of two feet or less in each direction around the ship, grid stretching was used to enlarge the domain. So far both mean flow and NLDE simulations were based on the same grid in order to avoid three dimensional interpolation. In fact, the NLDE needs much fewer grid points than CFL3D.

### Mean flow simulation

NASA Langley and Ames research centers have devoted significant resources in the past decades to developing modern CFD technology. The CFL3D 5.0 package from NASA Langley is used here to simulate the mean flow which will be given as a background flow to the unsteady flow computation of NLDE. The code is a Reynolds-Averaged thin-layer Navier-Stokes flow solver for structured grids. A finite volume algorithm with a spatial-factored diagonalised, implicit scheme is used in discretization of the partial differential equations. The upwind-biased-differencing using the flux-difference-splitting technique is employed.

From the experimental results, it is known that the flow is mostly separated, with free vortices originating from the sharp corners. There are two types of separation: one due to viscosity and the other due to sharp corners of the blocked structures. The former is heavily influenced by the Reynolds number. The latter is purely an inviscid phenomenon, independent of Reynolds number. The air wake is greatly influenced by both of them. In this mean flow simulation, we are concerned primarily with the inviscid phenomenon and used the Euler solver of CFL3D. The TTCP ship computational domain is divided into 10 blocks.

The Mach number chosen for the simulation is a high wind case. The incoming flow speed is 41 knots. The water surface is assumed to be a hard wall boundary. Fig. 7 shows the contour plot of velocity magnitude on the surface of TTCP ship. This is a zero yaw angle case from CFL3D results. The asymmetry property of zero yaw angle flow is captured very well. The flow is accelerated around the sharp corners and there are several reverse flow regions near the walls close to each corner. After the blocked structures there is massive flow separation; the separation line is clearly shown after each block.

Of importance to the landing operation is the flow condition over the flight deck. Fig. 8 depicts the contour

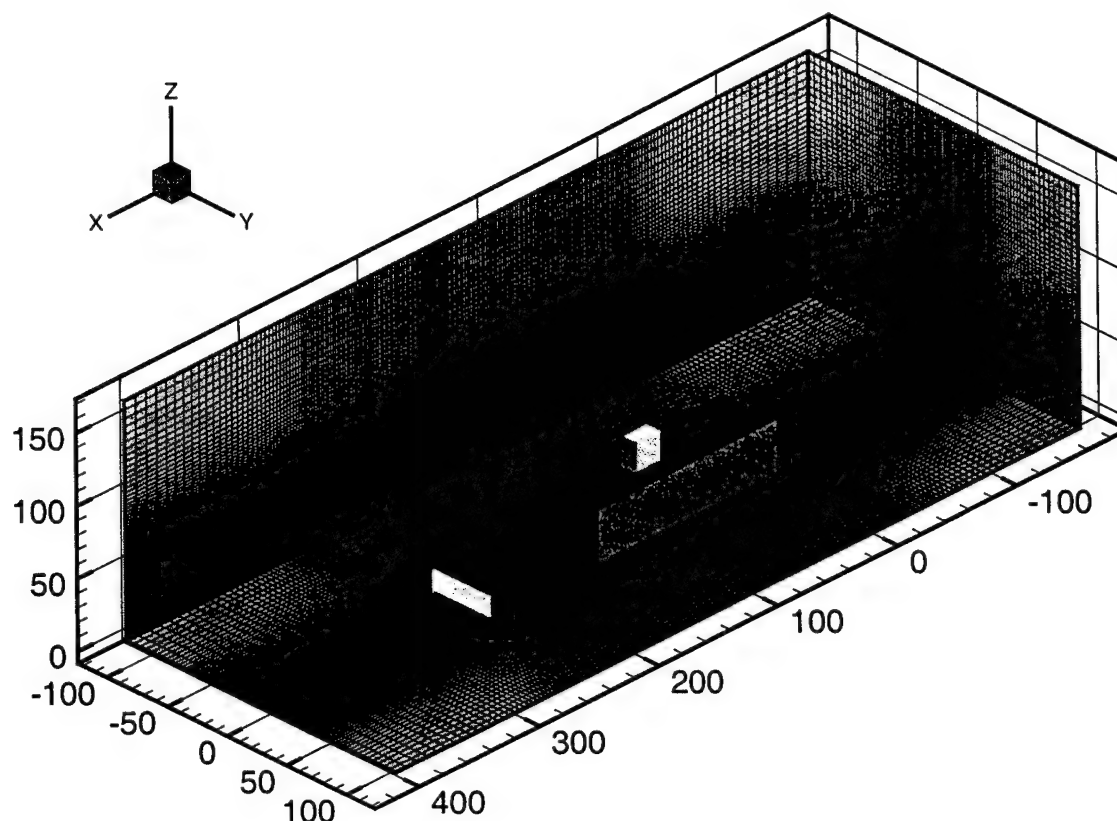


Figure 6: Configuration of TTCP ship and computational mesh

of velocity magnitude at the ship's center plane. It is shown that the large region of recirculating flow extends over the flight deck and rises higher than the hangar. This flow region is in the landing path.

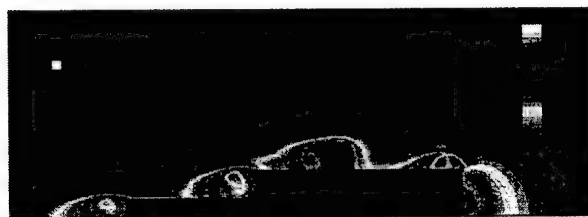


Figure 8: Flow speed contour on center plane of the TTCP ship

Fig. 9 shows velocity vectors in two horizontal planes 4.75 feet and 8.75 feet above the flight deck. Our numerical results are compared with a flow pattern obtained from an experimental study<sup>17</sup> in fig. 10. It shows the flow pattern from experiments, where four distinct flow regions are behind the hangar. This three dimensional vortex and reverse flow has very low speed but generally

is very unsteady and yaw-dependent. Comparing to the experiment, the physical flow features are well captured by the simulation. In the numerical plots, the vortex pair in the higher plane is much close to the center line and the hangar. This indicates that there is a horse shoe vortex as shown by the topological drawing in fig. 10.

In fig. 11 the velocity vector on the deck floor is compared with flow visualization results for the TTCP ship.<sup>23</sup> There are differences in the attachment point and the position of vortex center. This is probably due to our inviscid approach.

Based on the discussion above, in fact, the flow pattern shown represents a very rough mean of the flow. They are intended only to give approximate envelopes for the different regions and provide the background flow for NLDE simulations. There are wild fluctuations about this mean flow. The flow field is generally very unsteady. In the following section, the results from NLDE simulations are discussed based on this mean flow.

Finally in fig. 12 the performance of CFL3D (a serial code) is shown. For this TTCP ship configuration it takes days to get the steady state results.

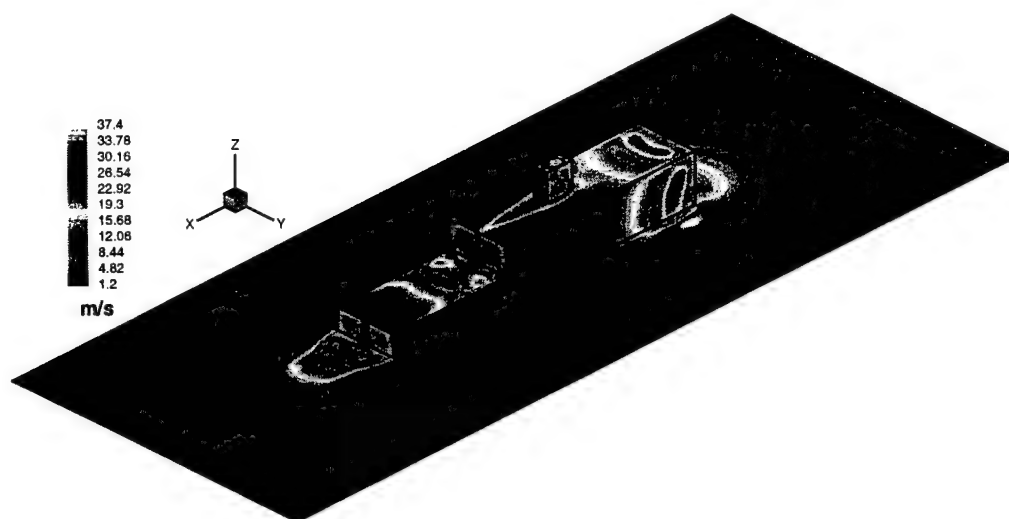


Figure 7: Flow speed contour on the surface of TTCP ship

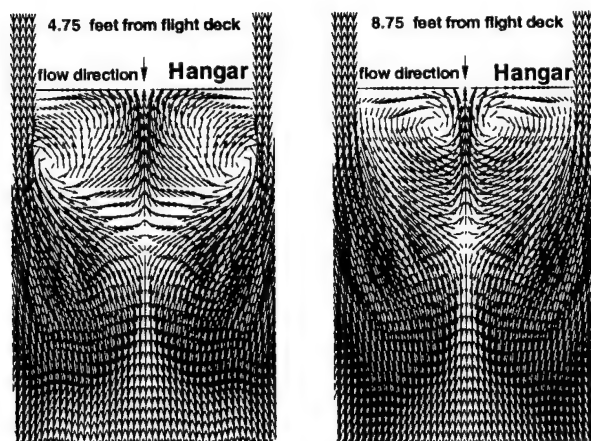


Figure 9: Flow velocity vectors at two horizontal planes over flight deck

### Perturbation simulation

As mentioned before, NLDE has been developed for solving more complex geometries, such as the TTCP ship, which allow multi-solid-boxes inside the computational domain. This makes the boundary condition implementation difficult, especially combined with a domain decomposition parallel technique. To overcome this difficulty, a single block domain was chosen for the NLDE code. The TTCP ship is divided into 88 solid boxes. Characteristic boundary conditions are used at the surfaces, edges and corners of these boxes. At each time step, after the single block computation is finished, the solid box wall boundary conditions are applied to update the value at wall grid points.

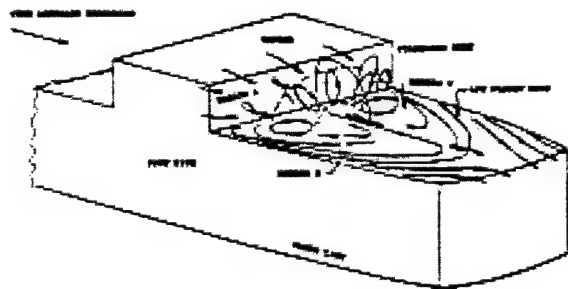


Figure 10: Topological drawings from experimental study<sup>17</sup>

The high wind speeds relevant to the ship/helicopter interface problem arise from storm centers far from the actual ship and are called neutrally stratified. This wind condition is considered at our inflow boundary. The principal parameters of the freestream airflow are (1) the mean windspeed, time-averaged over an appropriate scale; (2) the turbulence intensity; (3) the longitudinal (or integral) length scale of the turbulent velocity fluctuations. Empirical relationships are available (ESDU data items 74030, 74031) for the above four parameters as a function of the mean windspeed, elevation and roughness length scale.<sup>3</sup>

Incoming characteristics with source terms are introduced from the inflow boundary as it is expressed as  $L_i$  in equation (17) - (21). The magnitude of the incoming disturbance is determined by the turbulence intensity. Its spectrum is obtained from the wind spectrum by using a random walk (random phase) technique.

Fig. 13 and fig. 14 give contour plots of longitudinal

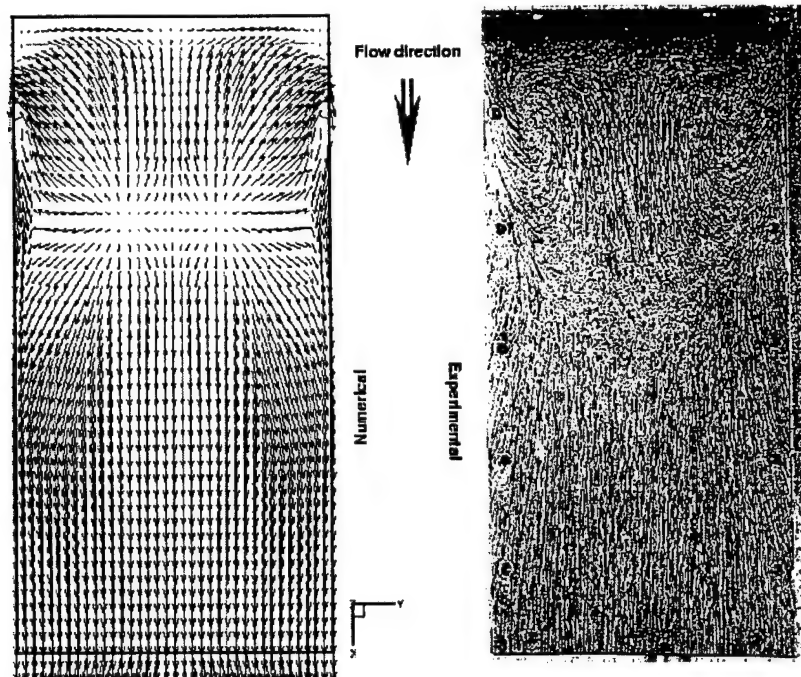


Figure 11: Predicted surface flow velocities compared to surface oil flow images<sup>23</sup>

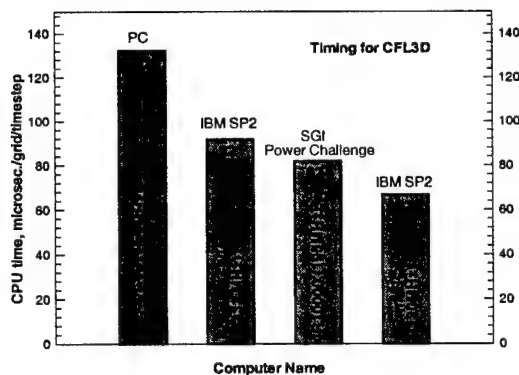


Figure 12: Timing for CFL3D on several computers

velocity perturbations  $u'$  in the center plane at two different timesteps. Fig. 15 gives contour plots of the longitudinal velocity intensity  $\sqrt{u'^2}$ . From this unsteady result, it is shown that large perturbations occur around the TTCP ship structure, especially in the area after the hangar and after the leading edge. In the field far from the ship the flow is quite steady. Vortex shedding from

the hangar can be clearly observed.

In fig. 16 and fig. 17, contour plots of vertical and transverse perturbation velocity  $v'$ ,  $w'$  are shown. In fig. 18 the vertical perturbation intensity  $\sqrt{w'^2}$  is given in the center plane. High instantaneous vertical perturbations are found in the region just after the hangar trailing edge. Since this is a zero yaw angle case, the transverse perturbation is quite weak over the flight deck. By comparing the instantaneous perturbations in fig. 13 and 17, the perturbation length scale of longitudinal perturbations is different from that of vertical perturbations.

The unsteady three-dimensional flow is of interest throughout the domain but in particular the flow unsteadiness is important around the helicopter landing deck. Fig. 19 presents a contour plot of perturbation intensity in a horizontal plane 17 feet above the deck, where the helicopter rotor would be.

From those preliminary results, the unsteady features of TTCP ship air wake are captured qualitatively. However, detailed experimental data is not yet available. In the meantime, the NLDE code is being improved and prepared for quantitative evaluation and analysis.

## Concluding Remarks

This paper presents steady and unsteady flow field



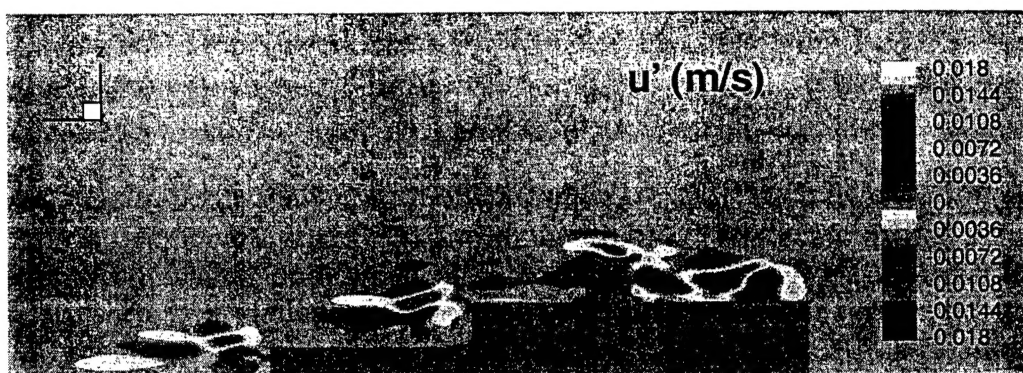


Figure 13: Contour of instantaneous longitudinal velocity perturbations at  $t = t_1$



Figure 14: Contour of instantaneous longitudinal velocity perturbations at  $t = t_2$

predictions for frigate class ships. A nonlinear disturbance equation solver has been developed using parallel computers. The parallel performance of the code has been compared on various computers. Our present results are qualitatively correct, and show that the key flow phenomena can be captured by using a steady-state code followed by the NLDE code. Future work will concentrate on more detailed comparisons to experiment, the inclusion of more geometrical features of the ships, and the inclusion viscous effects.

### Acknowledgments

We gratefully acknowledge ONR Grant No. N00014-97-1-0530. We would also like to thank Steve Zan (NRC Canada) and Kurt Long (USN Pax River).

### References

- [1] Bruner, C.W.S. and R.W. Walters, "Parallelization of the Euler Equations on Unstructured Grids", AIAA 97-1894.
- [2] Carico, D., Reddy, B., and Dimarzio, C., "Ship Airwake Measurements and Modeling Options for Rotorcraft Applications," In: Aircraft Ship Operations, AGARD CP-509, November 1991.
- [3] ESDU Data Items 74030, 74031, Engineering Sciences Data Unit International, McLean, VA.
- [4] Funk, J.D. and T. A. Egolf, "A Comparison of Helicopter Rotor Inflow Predictions in Turbulence using Blade Element and Vortex Lattice Models," Proceedings of the 50th American Helicopter Society Forum, Washington, D.C., May, 1994.
- [5] Healey, J. Val., "The Prospects for Simulating the Helicopter/Ship Interface," Naval Engineers Journal, March 1987, pp. 45-63.
- [6] Johns, M.K. and J. Val Healey, "The Airwake of a DD-963 Class Destroyer," Naval Engineers Journal, May, 1989.
- [7] Healey, J. Val., "Establishing a Database for Flight in the Wake of Structures," Journal of Aircraft, Vol. 29, No.4, July-Aug. 1992, pp. 559-564.
- [8] Hurst, D. W., and Newman, S.J., "Wind Tunnel Measurements of Ship Induced Turbulence and the



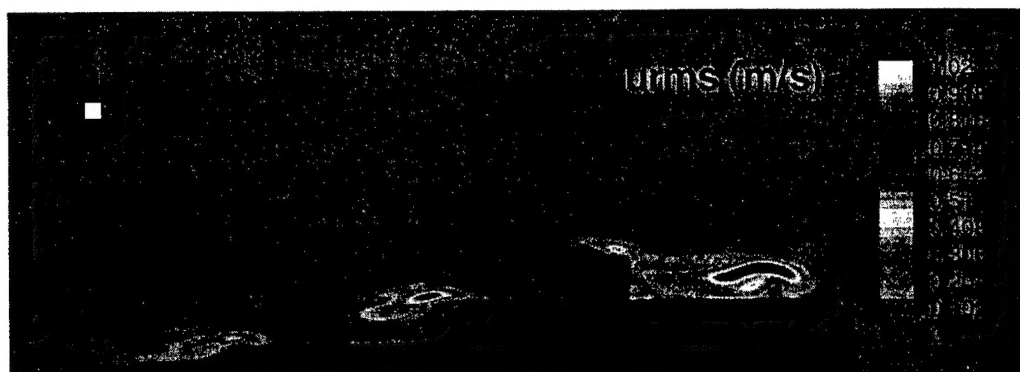


Figure 15: Contour of longitudinal velocity intensity

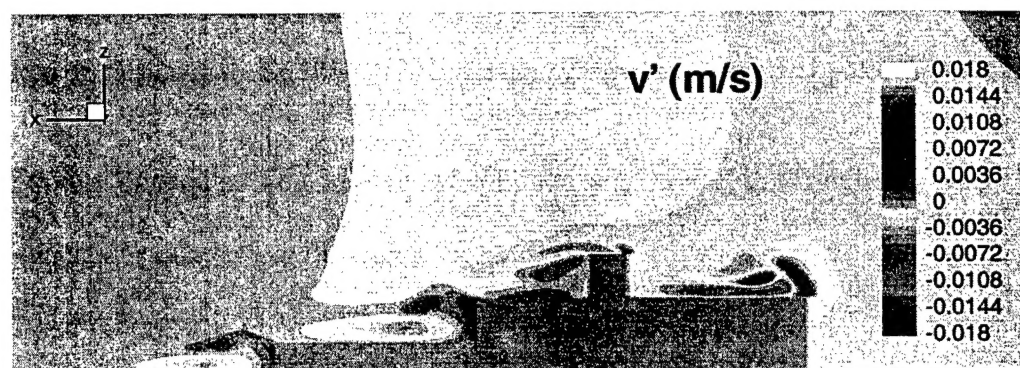


Figure 16: Contour of instantaneous transverse velocity perturbations

- Prediction of Helicopter Rotor Blade Response," Vertica, Vol. 12, No.3, 1988, pp. 267-278.
- [9] Geyer, W.G., J. Keller, and E.C. Smith, "Validation and Application of a Transient Response Analysis for Shipboard Engage/Disengage Operations," Proceedings of the 52nd American Helicopter Society Forum, Washington, D.C., June, 1996.
  - [10] Keller, J. and E.C. Smith, "Experimental / Theoretical Correlation of Analysis for Helicopter Blade-Droop Stop Impacts," submitted for publication in the Proceedings of 38th AIAA/ASME/ASCE/AHS/ASC Structure, Structural Dynamics, and Materials Conference, Orlando, April, 1997.
  - [11] Williams, S. and Long, K.R., "Dynamic Interface Testing and the Pilots Rating Scale," The 53rd AHS Forum, April, 1997.
  - [12] Landsberg, A.M., Young, T.R., Jr. and Boris, J.P., "An efficient, Parallel Method for Solving Flows in Complex Three-Dimensional Geometries", 32nd Aerospace Sciences Meeting & Exhibit, January 10-13, 1994, Reno, NV.
  - [13] Landsberg, A.M., W.C. Sandberg, T.R. Young, and J.P. Boris, "DDG-51 Flt-IIA Airwake Study, Part 2: Hangar Interior Flow," NRL/MR/6410-96-7898, Nov., 1996
  - [14] Morris P.J., Long L.N., Bangalore A. and Wang Q., "A Parallel Three-Dimensional Computational Aeroacoustics Method Using Non-Linear Disturbance Equations", J. Computational Physics, 1997 and AIAA 97-1598.
  - [15] Pacheco, P.S., "Parallel Programming with MPI," Morgan Kaufmann, San Francisco, 1997
  - [16] Prasad, J.V.R., Mavris, D.N., and Schrage, D. P., "Ship Airwake Modeling and Simulation, Phase I: Methodology Development," Research Report submitted to Naval Air Warfare Center, School of Aerospace Engineering, Georgia Institute of Technology, Atlanta, August 1992.
  - [17] Rhoades, M. M., and Healey, J. Val., "Flight Deck Aerodynamics of a Nonaviation Ship," Journal of Aircraft, Vol. 29, No.4, July-August 1992, pp. 619-626.

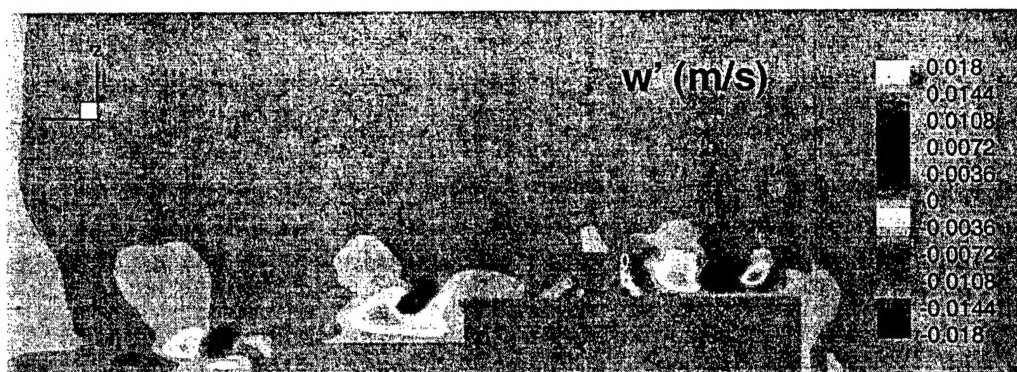


Figure 17: Contour of instantaneous vertical velocity perturbations

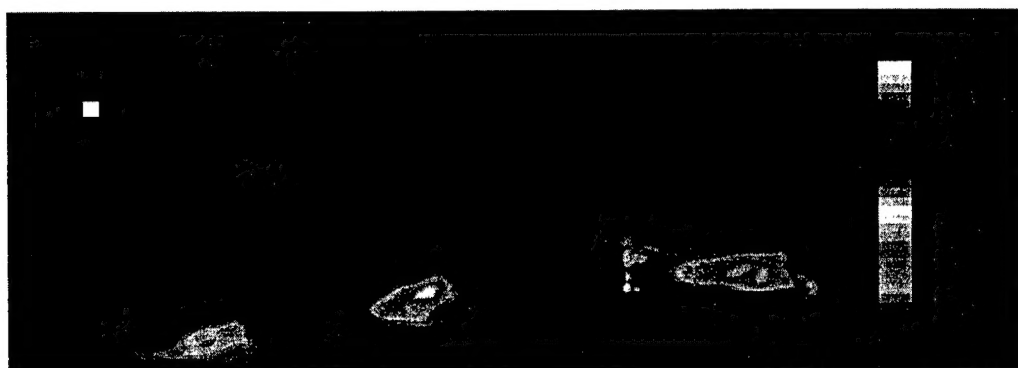


Figure 18: Contour of vertical velocity intensity

- [18] Krist, S.L., R.T. Biedron, and C.L. Rumsey, "CFL3D User's Manual (Version 5.0)," NASA Langley, Nov., 1996.
- [19] Tai, T.C. and Carico, D., "Simulation of DD-963 Ship Airwake by Navier-Stokes Method," AIAA 93-3002.
- [20] Tam C.K.W., and Webb, J.C., "Dispersion-Relation-Preserving Finite Difference Schemes for Computational Aeroacoustics," J. of Computational Physics, Vol.1, 1993.
- [21] Thompson K.W., "Time-Dependent Boundary Conditions for Hyperbolic System", J. of Computational Physics 89, 1990.
- [22] Zan, S.J. and E.A. Garry, "Wind Tunnel Measurements of the Airwake Behind a Model of a Generic Frigate," NRC-CNRC Report LTR-AA-13, June, 1994.
- [23] Zan, S.J., Unpublished data from the Aerodynamics Laboratory, Institute for Aerospace Research, National Research Council of Canada, 1998.

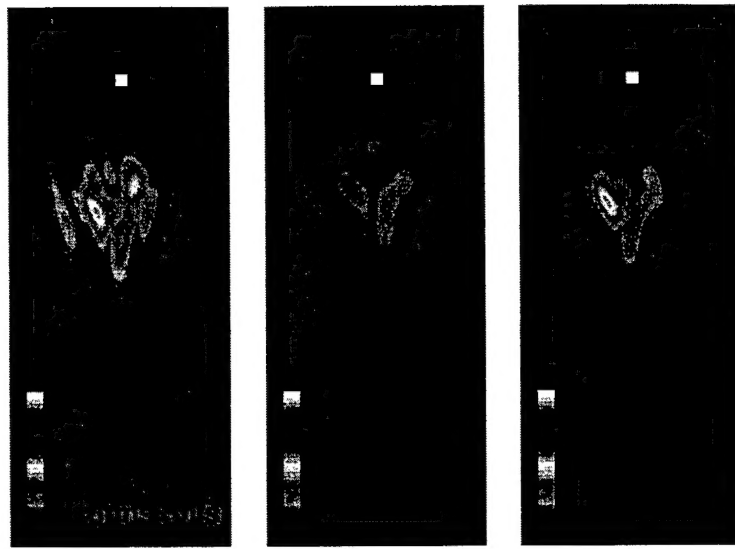


Figure 19: Contour plots of perturbation velocity intensity in the rotor plane of helicopter